



Universidad Autónoma  
de Madrid

**Biblos-e Archivo**  
Repositorio Institucional UAM

**Repositorio Institucional de la Universidad Autónoma de Madrid**

<https://repositorio.uam.es>

Esta es la **versión de autor** del artículo publicado en:  
This is an **author produced version** of a paper published in:

Chemical Communications 56.8 (2020): 1267-1270

**DOI:** <https://doi.org/10.1039/c9cc06479f>

**Copyright:** © 2020 The Royal Society of Chemistry

El acceso a la versión del editor puede requerir la suscripción del recurso

Access to the published version may require subscription

# Oxygen Reduction Using a Metal-Free Naphthalene Diimide-Based Covalent Organic Framework Electrocatalyst.

Sergio Royuela,<sup>‡ab</sup> Emiliano Martínez-Periñán,<sup>‡c</sup> Marina P. Arrieta,<sup>a</sup> José I. Martínez,<sup>d</sup> M. Mar Ramos,<sup>b</sup> Félix Zamora,<sup>\*efgh</sup> Encarnación Lorenzo<sup>\*cfg</sup> and José L. Segura<sup>\*a</sup>

DOI: 10.1039/c9cc06479f

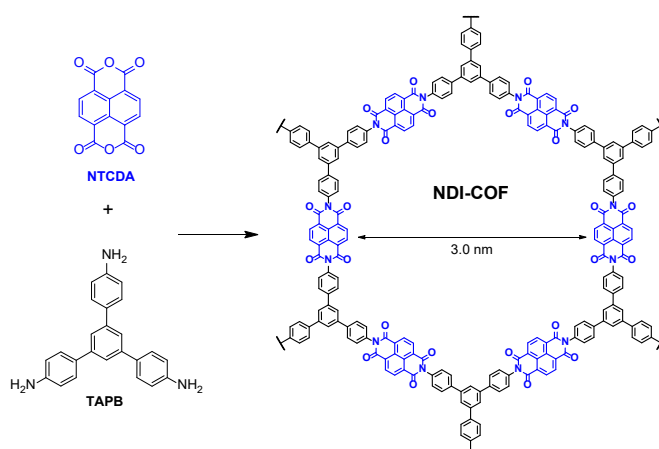
## ABSTRACT

**A novel naphthalene diimide-based covalent organic framework (NDI-COF) has been synthesized and successfully exfoliated into COF nanosheets (CONs). Electrochemical measurements reveal that the naphthalene diimide units incorporated into NDI-CONs act as efficient electrocatalysts for oxygen reduction in alkaline media, showing its potential for the development of metal-free fuel cells.**

Platinum and platinum-containing compounds have long been regarded as the best catalysts for the oxygen reduction reaction (ORR), the key electrochemical process in fuel cells,<sup>1, 2</sup> since they allow the reaction mechanism to occur *via* a 4-electron pathway.<sup>3</sup> However, the growing energy demands and the limited reserves of Pt in nature, together with its high cost, have led to the development of a new generation of fuel cells based on other transition metals or organic materials.<sup>4</sup> Initially, non-noble metal-based catalysts were explored to replace Pt based materials. Thus, transition-metal-coordinated nitrogen-doped carbon catalysts have attracted great attention as ORR electrocatalyst in alkaline electrolytes.<sup>5</sup> More recently, metal-free porous materials including nitrogen-doped carbon materials such as porous polymers,<sup>6</sup> covalent triazine frameworks (CTFs),<sup>7</sup> N-doped graphene<sup>8</sup> and N-doped ordered mesoporous graphitic arrays,<sup>6</sup> have been explored, owing to their high catalytic activity and good durability.

Nowadays, covalent organic frameworks (COFs) have come forth as alternative nanometer-scale porous frameworks with promising properties in several fields.<sup>9, 10</sup> COFs offer predictive design criteria to organize redox-active groups into crystalline and high surface-area

polymer networks that adopt two-dimensional (2D) layered structures.<sup>11</sup> Chemically robust COFs have been obtained using linkages such as imines,<sup>12</sup>  $\beta$ -ketoenamines<sup>13</sup> and imides.<sup>14</sup> In this sense, imide-based polymers are known for their high thermal stability, good chemical resistance, and outstanding electrochemical properties.<sup>15</sup> Among imide derivatives, naphthalene diimides (NDI) have been considered as promising electron acceptors in organic field-effect transistors (OFETs)<sup>16</sup> and complex supramolecular structures.<sup>17</sup> Nevertheless, reports of naphthalene diimide-based COFs are still very scarce in the literature and to the best of our knowledge limited to only three examples.<sup>18-20</sup>



**Scheme 1** Schematic representation of the synthesis of **NDI-COF**.

In this work, a new 2D imide-based COF containing electrochemically active NDI units in its structure, **NDI-COF**, has been synthesized and further exfoliated into COF nanosheets (CONs). Incorporating NDI as an electron-poor building block makes the material energetically favourable to accept electrons from oxygen. This allows the direct use of **NDI-COF** as a suitable ORR catalyst, unlike previously studied COFs which require a combination with metal species and/or an additional pyrolysis process.<sup>21-23</sup>

**NDI-COF** was synthesized by condensation reaction between 1,4,5,8-naphthalenetetracarboxylic dianhydride (NTCDA) and 1,3,5-tris(4-aminophenyl)benzene (TAPB) under solvothermal conditions by heating the mixture at 120 °C for 4 days (Scheme 1). The resulting solid was washed and activated with supercritical CO<sub>2</sub> to give a light brown solid of **NDI-COF** (see the ESI for details). Fourier-transform infrared spectroscopy (FTIR) analysis of **NDI-COF** showed the

presence of the characteristic bands from the six-membered imide ring. Thus, the bands at 1715 and 1675  $\text{cm}^{-1}$  correspond to the asymmetric and symmetric stretching vibrations of the C=O group, while the band at 1340  $\text{cm}^{-1}$  is assigned to the C-N-C stretching vibration.<sup>18, 20</sup> Furthermore, the spectrum does not show the presence of the N-H or C=O bands from the amino and anhydride monomers, nor the intermediate amic amid C=O band around 1650  $\text{cm}^{-1}$  (Fig. S1 and S2). The solid state  $^{13}\text{C}$  cross-polarization magic angle spinning NMR ( $^{13}\text{C}$ -CP/MAS-NMR) spectrum of **NDI-COF** shows a signal at 164.4 ppm corresponding to the carbonyl carbon of the six-membered imide ring (Fig. 1a). Two additional overlapping signals centered at 143.3 and 129.5 ppm were assigned to the aromatic carbons from the naphthalenyl and phenyl moieties. The formation of a crystalline material was confirmed by powder X-ray diffraction (PXRD) and *in silico* experiments performed using the Gaussian09,<sup>24</sup> and CASTEP<sup>25</sup> software packages. Four structural models, the eclipsed stacking (AA), the staggered stacking (AB), and two intermediate situations with partial layer offsets were modelled (see ESI for details). PXRD of **NDI-COF** shows three diffraction peaks at 3.0°, 5.7° and 7.3°, which correspond to the (100), (200) and (210) facets, respectively (Fig. 1b). The experimental data agrees best with the simulated eclipsed model with a 1/6 layer offset and Pawley refinement produced a hexagonal unit cell with  $a = b = 36.019 \text{ \AA}$ ,  $c = 7.086 \text{ \AA}$ ,  $\alpha = \beta = 90^\circ$  and  $\gamma = 120^\circ$ , with refinement results of  $R_{\text{wp}} = 6.05 \%$  and  $R_{\text{p}} = 4.00 \%$ . The porosity of **NDI-COF** was investigated by  $\text{N}_2$  sorption isotherms at 77 K (Fig. 1c), from which a Brunauer-Emmett-Teller (BET) surface area of  $1138 \text{ m}^2\text{g}^{-1}$  and a total pore volume of  $0.777 \text{ cm}^3\text{g}^{-1}$  were derived. The pore size distribution calculated by non-local density functional theory (NLDFIT) is centered at 2.5 nm, which agrees with the expected value from the layer offset model. Finally, the thermal stability of **NDI-COF** was studied by thermogravimetric analysis (TGA) revealing that the material is stable up to 500 °C (Fig. S4).

The presence of the electroactive NDI moiety in the **NDI-COF** structure prompted us to study it as ORR electrocatalyst. To this end, we first addressed the issue of the COF processability to get a suitable material dispersion in the electrode. In that sense, liquid phase exfoliation (LPE) assisted by sonication is an easy and scalable method to disrupt the non-covalent interactions between COF layers and produce COF nanosheets (CONs).<sup>26</sup> In fact, by

simple varying the processing conditions (solvent, power, time, etc.), different 2D-COFs have been successfully exfoliated,<sup>27</sup> even in water.<sup>28</sup> Thus, the LPE conditions for water based **NDI-CONs** colloids were optimized (see the ESI for details). The colloidal character of the resulting suspension was corroborated by the Tyndall effect upon irradiation with a laser beam (inset Fig. 2a). The hydrodynamic sizes of the **NDI-CONs** were determined by dynamic light scattering (DLS) measurements showing mainly a monomodal size distribution of ca. 690 nm (Fig. 2a). Transmission electron microscopy (TEM) (Fig. 2b and S5) evidenced the formation of thin transparent layers and their selected area electron diffraction (SAED) pattern (inset Fig. 2b) gave further evidence of the crystallinity of **NDI-CONs**. Fig. 2c shows an atomic force microscopy (AFM) topographic image of water **NDI-COF** colloids deposited by drop-casting onto SiO<sub>2</sub> in which nanosheets with lateral dimensions of hundreds of nanometers and an average apparent height of 6-7 nm are observed (Fig. S6).

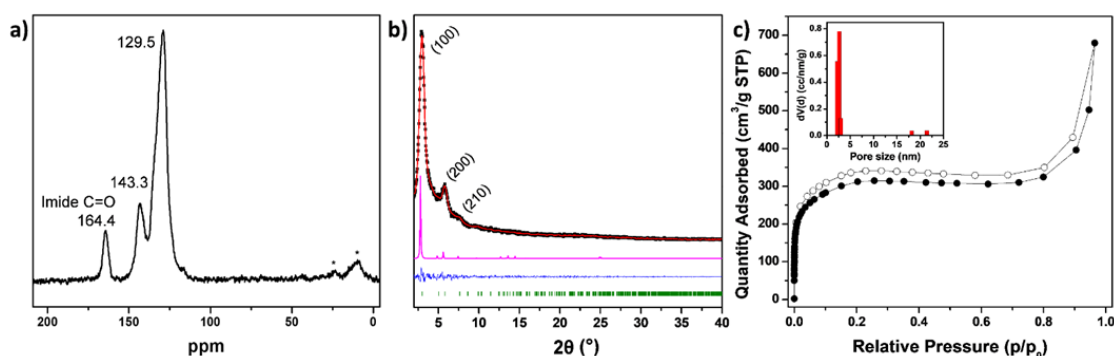


**Fig. 1** a) <sup>13</sup>C-CP/MAS-NMR spectrum of **NDI-COF**. Asterisks indicate spinning side bands. b) PXRD analysis of **NDI-COF**: experimental (black), Pawley refined (red), difference (blue), simulated using AA stacking mode with a 1/6 layer offset (pink). Reflection positions are shown by tick marks. c) N<sub>2</sub> sorption isotherms for **NDI-COF**. Inset shows the pore size distribution calculated by NLDFT.

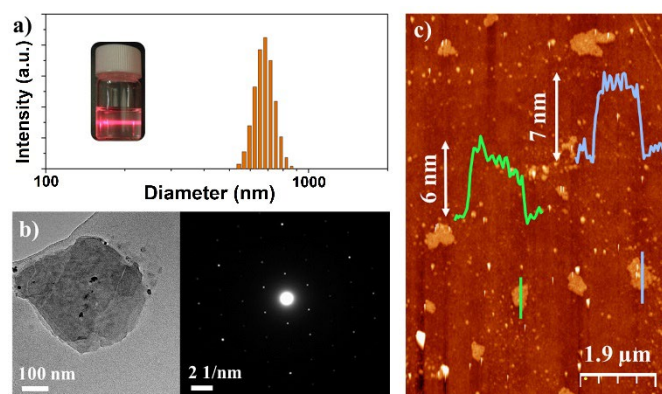


**Fig. 2** Characterization of **NDI-CONs**: a) DLS measurement and Tyndall effect (inset). b) TEM image and SAED analysis (inset). c) AFM topography image of several **NDI-CONs** deposited on  $\text{SiO}_2$  and their height profiles (insets).

The **NDI-CONs** colloids were then drop-casted onto glassy carbon electrodes (GC) and used to test the ORR electrocatalytic activity of this nanomaterial, hereafter termed **NDI-CON/GC**. For this purpose, static and hydrodynamic electrochemical measurements were carried out using 0.1 M NaOH as supporting electrolyte. As a first step, we characterized the electrochemical behaviour of **NDI-CON/GC** in the absence of oxygen (Fig. S13a, red curve), in order to ascertain the electrochemical processes that are taking place at the nanomaterial-modified electrode during the applied scan potential. As can be observed, in the first cathodic scan a reduction peak appears at -0.38 V vs. SCE. This process is ascribed to the electrochemical reduction of the electroactive NDI moiety. A small oxidation peak is detected in the backward anodic scan, which corresponds to the oxidation of the reduced specie generated in the cathodic scan in a quasi-reversible redox process. The lack of total reversibility can be a consequence of the modest electrically conducting behaviour of COF materials.<sup>29</sup> It can also be observed how the capacitance current increases compared with the bare GC electrode's cyclic voltammetry (Fig. S13, black curve). This fact is a clear consequence of the electroactive area increase due to the 2D structure of the exfoliated **NDI-COF**.<sup>30, 31</sup>

Once the electrochemical behaviour of **NDI-CON/GC** had been established, we proceeded to study its response in the presence of oxygen (saturated  $\text{O}_2$  0.1 M NaOH solution). As can be seen in Fig. 3a, red curve, the potential of the  $\text{O}_2$  reduction wave clearly shifts

towards more positive values compared with the bare GC electrode. The oxygen reduction in this case takes place at the same potential at which the NDI moiety is reduced, as has been proved with the modification of a bare GC electrode with the NDI-monomer (Fig. 3a, blue curve). The good redox activity and semiconducting nature of the NDI motive<sup>32</sup> may facilitate the electron transfer to oxygen speeding up the sluggish kinetics of oxygen reduction and therefore catalyzing the ORR.<sup>33</sup> As consequence, the current intensity increases compared to the bare GC electrode, which confirms the great trend of **NDI-CONS** to assist the ORR. SEM (Fig. S14) and AFM images (Fig. S15) revealed that **NDI-CON** did not suffer any morphological changes after catalysis.

In order to determine the number of electrons involved in the electrochemical process the hydrodynamic electrochemical response of an **NDI-CONS** modified electrode was studied at a GC disk-Pt ring electrode (Fig. 3b). The calculated value of near 3.6 is significantly higher to that calculated for the bare GC electrode, ca. 2.4 (Fig. S16). Based on the described mechanism for ORR in basic medium, the value of 3.6 indicates that the process has two contributions but with a clear preference for the desired 4-electron pathway.<sup>34</sup> This fact makes **NDI-CON** an attractive material for anion-exchange membrane fuel cells (AEMFCs).

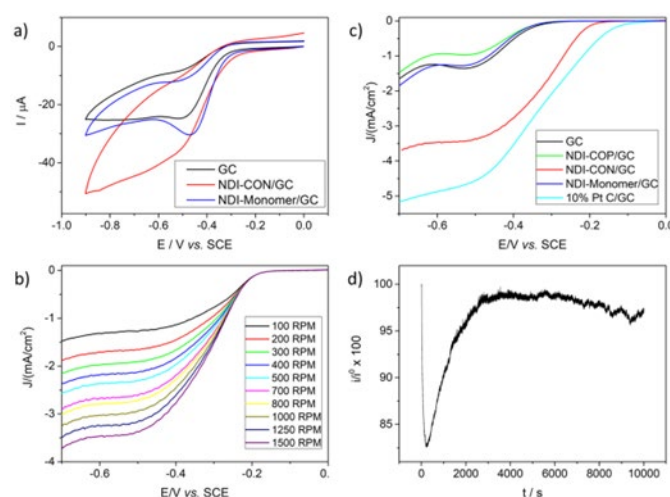


**Fig. 3** a) Cyclic Voltammetry of GC electrode (black), **NDI-CON/GC** electrode (red) and NDI-monomer/GC electrode (blue) in 0.1 M NaOH O<sub>2</sub> saturated solution. b) Hydrodynamic linear sweep voltammetry of **NDI-CON/GC** in 0.1 M NaOH O<sub>2</sub> saturated solution at different rotation rates and 10 mV/s. c) Hydrodynamic linear sweep voltammetry of GC (black), **NDI-CON/GC** (red), **NDI-**

***polymer/GC** (green), **NDI-monomer/GC** (blue) and 10% Pt C/GC (cyan) electrodes in 0.1 M NaOH O<sub>2</sub> saturated solution at 1500 rpm and 10 mV/s. d) Current intensity stability of **NDI-CON/GC** electrode operating in 0.1 M NaOH O<sub>2</sub> saturated solution at a constant potential (- 0.5 V vs. SCE).*

Intrigued by the potential influence of the **NDI-COF** ordered structure in these results we prepared and evaluated the electrochemical response of a GC electrode modified with the same amount of an equivalent amorphous **NDI-polymer** (see the ESI for details). In this case, the material does not present a two-dimensional layered structure, and therefore the porosity is really low compared to that of **NDI-COF**. The hydrodynamic electrochemical behaviour of the **NDI-CON/GC** disk electrode was compared with those of the bare GC electrode, the **NDI-polymer**-modified GC electrode and a 10% Pt supported on carbon modified GC electrode (Fig. 3c). The effect of **NDI-CONS** on ORR is clearly demonstrated if we compare the onset potential of the bare GC (-0.37 V vs. SCE) and **NDI-CON/GC** (-0.25 V vs. SCE) electrodes. A potential shift of 120 mV toward positive potential clearly improves the electrochemical process with respect to the unmodified GC electrode. In contrast, **NDI-polymer/GC** performs worse as ORR electrocatalyst, as can be observed in Fig. 3c. In this sense, the lack of well-defined pores in **NDI-polymer** avoids O<sub>2</sub> diffusion and its insulating properties, compared to the bare GC electrode, determine its poor electrocatalytic performance. This result shows how a change in the microstructure of the material dramatically affects its electrocatalytic activity towards the ORR and the relevant role that the COF's ordered structure plays in the electrochemical process.

To complete the electrochemical characterization of the **NDI-CON/GC** electrode, the stability of the current intensity in operational conditions was tested. Fig. 3d shows that during the first seconds, the current decreases down to 83 % of its initial value as consequence of the discharge of the double layer generated by the electrode polarization and the reduction of O<sub>2</sub> molecules that initially are adsorbed on the electrode. Nevertheless, after *ca.* 3000 seconds almost 100 % of the initial current is recovered, due to the **NDI-CON** activation during the electrocatalyst process. Therefore, **NDI-CON**



requires ca. 3000 seconds to activate itself in the best operational conditions. Then, the current keeps almost constant for 10000 s, which is the maximum time assayed, losing only ca. 3 % of its initial value. It is also worth mentioning that the material has a strong tolerance to methanol crossover (Fig. S17), which represents an important advantage over platinum-based ORR electrocatalysts.

In summary, it should be highlighted that although there are some materials that cause a potential shift of the ORR process towards more positive values than that described in this work, either they contain metals in their structure,<sup>22</sup> require an additional pyrolysis step before being applied,<sup>23</sup> or in some cases are used in combination with other conductive nanomaterials.<sup>35</sup> Therefore, some important benefits of the new **NDI-COF** synthesized here are that it is not only metal free, but also no additional pyrolysis process has to be applied before its use. Instead, the electrocatalytic activity is a consequence of the specific electroactive moiety selected for the design of this new COF electrocatalyst. Even more, as far as we know, in this work we describe for the first time that the electroactive moiety of a COF is responsible of its ORR electrocatalytic activity. This finding opens a new research field on how the electrochemical properties of COF precursors may affect the electrocatalytic behaviour of the final material for different applications.

*Financial support from the Spanish Government (projects MAT2016-77608-C3-1-P, MAT2016-77608-C3-2-P, CTQ2017-84309-C2-1-R, MAT2017-85089-C2-1-R, FJCI-2017-33536 and RYC-2015-17730), the UCM (INV.GR.00.1819.10759) and the Madrid Regional Government (TRANSNANOAVANSENS-CM (S2018/NMT-4349)) is acknowledged.*

## **Conflicts of interest**

There are no conflicts to declare.

## **Notes and references**

- 1 J. Wu and H. Yang, *Acc. Chem. Res.*, 2013, **46**, 1848-1857.
- 2 M. Shao, Q. Chang, J.-P. Dodelet and R. Chenitz, *Chem. Rev.*, 2016, **116**, 3594-3657.
- 3 E. Martínez-Periñán, I. Bravo, S. J. Rowley-Neale, E. Lorenzo and C. E. Banks, *Electroanal.*, 2018, **30**, 436-444.
- 4 G. Wu and P. Zelenay, *Acc. Chem. Res.*, 2013, **46**, 1878-1889.
- 5 M. Zhou, H.-L. Wang and S. Guo, *Chem. Soc. Rev.*, 2016, **45**, 1273-1307.
- 6 Z. Xiang, Y. Xue, D. Cao, L. Huang, J.-F. Chen and L. Dai, *Angew. Chem., Int. Ed.*, 2014, **53**, 2433-2437.
- 7 W. Yu, S. Gu, Y. Fu, S. Xiong, C. Pan, Y. Liu and G. Yu, *J. Catal.*, 2018, **362**, 1-9.
- 8 L. Qu, Y. Liu, J.-B. Baek and L. Dai, *ACS Nano*, 2010, **4**, 1321-1326.
- 9 M. S. Lohse and T. Bein, *Adv. Funct. Mater.*, 2018, **28**, 1705553.
- 10 S. P. S. Fernandes, V. Romero, B. Espiña and L. M. Salonen, *Chem. Eur. J.*, 2019, **25**, 6461-6473.
- 11 X. Zhan, Z. Chen and Q. Zhang, *J. Mater. Chem. A*, 2017, **5**, 14463-14479.
- 12 J. L. Segura, M. J. Mancheño and F. Zamora, *Chem. Soc. Rev.*, 2016, **45**, 5635-5671.
- 13 S. Kandambeth, A. Mallick, B. Lukose, M. V. Mane, T. Heine and R. Banerjee, *J. Am. Chem. Soc.*, 2012, **134**, 19524-19527.
- 14 Q. Fang, Z. Zhuang, S. Gu, R. B. Kaspar, J. Zheng, J. Wang, S. Qiu and Y. Yan, *Nat. Commun.*, 2014, **5**, 4503.
- 15 D.-J. Liaw, K.-L. Wang, Y.-C. Huang, K.-R. Lee, J.-Y. Lai and C.-S. Ha, *Prog. Polym. Sci.*, 2012, **37**, 907-974.
- 16 M. M. Durban, P. D. Kazarinoff and C. K. Luscombe, *Macromolecules*, 2010, **43**, 6348-6352.
- 17 E. Castaldelli, E. R. Triboni and G. J.-F. Demets, *Chem. Commun.*, 2011, **47**, 5581-5583.

- 18 L. Jiang, Y. Tian, T. Sun, Y. Zhu, H. Ren, X. Zou, Y. Ma, K. R. Meihaus, J. R. Long and G. Zhu, *J. Am. Chem. Soc.*, 2018, **140**, 15724-15730.
- 19 J. Lv, Y.-X. Tan, J. Xie, R. Yang, M. Yu, S. Sun, M.-D. Li, D. Yuan and Y. Wang, *Angew. Chem., Int. Ed.*, 2018, **57**, 12716-12720.
- 20 G. Wang, N. Chandrasekhar, B. P. Biswal, D. Becker, S. Paasch, E. Brunner, M. Addicoat, M. Yu, R. Berger and X. Feng, *Adv. Mater.*, 2019, **31**, 1901478.
- 21 W. Ma, P. Yu, T. Ohsaka and L. Mao, *Electrochem. Commun.*, 2015, **52**, 53-57.
- 22 D. Wu, Q. Xu, J. Qian, X. Li and Y. Sun, *Chem. Eur. J.*, 2019, **25**, 3105-3111.
- 23 Q. Xu, Y. Tang, X. Zhang, Y. Oshima, Q. Chen and D. Jiang, *Adv. Mater.*, 2018, **30**, 1706330.
- 24 M. J. Frisch, G. W. Trucks, H. B. Schlegel, G. E. Scuseria, M. A. Robb, J. R. Cheeseman, G. Scalmani, V. Barone, B. Mennucci, G. A. Petersson, H. Nakatsuji, M. Caricato, X. Li, H. P. Hratchian, A. F. Izmaylov, J. Bloino, G. Zheng, J. L. Sonnenberg, M. Had and D. J. Fox, Gaussian 09, Revision A.01, 2009.
- 25 J. Clark Stewart, D. Segall Matthew, J. Pickard Chris, J. Hasnip Phil, I. J. Probert Matt, K. Refson and C. Payne Mike, *Z. Kristallogr. Cryst. Mater.*, 2005, **220**, 567-570.
- 26 I. Berlanga, M. L. Ruiz-González, J. M. González-Calbet, J. L. G. Fierro, R. Mas-Ballesté and F. Zamora, *Small*, 2011, **7**, 1207-1211.
- 27 I. Berlanga, R. Mas-Ballesté and F. Zamora, *Chem. Commun.*, 2012, **48**, 7976-7978.
- 28 P. Albacete, A. López-Moreno, S. Mena-Hernando, A. E. Platero-Prats, E. M. Pérez and F. Zamora, *Chem. Commun.*, 2019, **55**, 1382-1385.
- 29 C. R. Mulzer, L. Shen, R. P. Bisbey, J. R. McKone, N. Zhang, H. D. Abruña and W. R. Dichtel, *ACS Cent. Sci.*, 2016, **2**, 667-673.
- 30 Poonam, K. Sharma, A. Arora and S. K. Tripathi, *J. Energy Storage*, 2019, **21**, 801-825.

- 31 J. Sun, A. Klechikov, C. Moise, M. Prodana, M. Enachescu and A. V. Talyzin, *Angew. Chem., Int. Ed.*, 2018, **57**, 1034-1038.
- 32 X. Guo, F. S. Kim, M. J. Seger, S. A. Jenekhe and M. D. Watson, *Chem. Mater.*, 2012, **24**, 1434-1442.
- 33 S. Roy, A. Bandyopadhyay, M. Das, P. P. Ray, S. K. Pati and T. K. Maji, *J. Mater. Chem. A*, 2018, **6**, 5587-5591.
- 34 D. R. Dekel, *J. Power Sources*, 2018, **375**, 158-169.
- 35 J. Guo, C.-Y. Lin, Z. Xia and Z. Xiang, *Angew. Chem., Int. Ed.*, 2018, **57**, 12567-12572.

Electronic supporting information

## **Oxygen Reduction Using a Metal-Free Naphthalene Diimide-Based Covalent Organic Framework Electrocatalyst**

Sergio Royuela,<sup>‡a,b</sup> Emiliano Martínez-Periñán,<sup>‡c</sup> Marina P. Arrieta,<sup>a</sup> José I. Martínez,<sup>d</sup> M. Mar Ramos,<sup>b</sup> Félix Zamora,<sup>\*e,f,g,h</sup> Encarnación Lorenzo<sup>\*c,f,g</sup> and José L. Segura<sup>\*a</sup>

<sup>a</sup> Departamento de Química Orgánica I, Facultad de CC. Químicas, Universidad Complutense de Madrid, 28040 Madrid, Spain.

<sup>b</sup> Departamento de Tecnología Química y Ambiental, Universidad Rey Juan Carlos, 28933 Madrid, Spain.

<sup>c</sup> Departamento de Química Analítica y Análisis Instrumental, Facultad de Ciencias, Universidad Autónoma de Madrid, 28049 Madrid, Spain.

<sup>d</sup> Departamento de Nanoestructuras, Superficies, Recubrimientos y Astrofísica Molecular, Instituto de Ciencia de Materiales de Madrid (ICMM-CSIC), 28049 Madrid, Spain.

<sup>e</sup> Departamento de Química Inorgánica, Facultad de Ciencias, Universidad Autónoma de Madrid, 28049 Madrid, Spain.

<sup>f</sup> Instituto Madrileño de Estudios Avanzados en Nanociencia (IMDEA-Nanociencia), Cantoblanco, 28049 Madrid, Spain.

<sup>g</sup> Institute for Advanced Research in Chemical Sciences (IAdChem), Universidad Autónoma de Madrid, 28049 Madrid, Spain.

<sup>h</sup> Condensed Matter Physics Center (IFIMAC), Universidad Autónoma de Madrid, 28049 Madrid, Spain.

<sup>‡</sup> These authors contributed equally to this work.

## General Methods

Thin layer chromatography (TLC) was performed using pre-coated silica gel 60 F254 and compounds were visualized under UV light ( $\lambda = 254$  nm). Solution  $^1\text{H}$  NMR and  $^{13}\text{C}$  NMR spectra were recorded on a Bruker AVIII-300 MHz spectrometer. Chemical shifts were reported in ppm and referenced to the residual non-deuterated solvent frequencies ( $\text{CDCl}_3$ :  $\delta$  7.26 ppm for  $^1\text{H}$ , 77.0 ppm for  $^{13}\text{C}$ ). Mass spectra were recorded by means of matrix-assisted laser desorption/ionization time-of-flight (MALDI-TOF) or fast atom bombardment (FAB) ionization techniques.

## Materials

The following reagents were commercially available and were used as received: 1,4,5,8-naphthalenetetracarboxylic dianhydride (NTCDA), p-nitroacetophenone, trifluoromethane-sulfonic acid, palladium on carbon (10 wt%), hydrazine hydrate (50-60 wt%), platinum on carbon (10 wt%). 1,3,5-tris-(4-aminophenyl)benzene (TAPB)<sup>1</sup> and *N,N'*-bis-(2-ethylhexyl)-1,4,5,8-naphthalene-tetracarboxydiimide (NDI-monomer)<sup>2</sup> were prepared according to previously reported procedures.

## Instrumental

- Fourier-transform infrared spectroscopy (FTIR). Solids were analysed by FTIR on a Bruker TENSOR 27 on a diamond plate (ATR).
- Powder X-ray diffraction (PXRD). PXRD measurements were carried out with X'PERT MPD with conventional Bragg-Brentano geometry using monochromatic Cu K $\alpha$ 1 radiation ( $\lambda = 1.5406$  Å) in the  $2\theta = 2^\circ - 40^\circ$  range.
- Solid state  $^{13}\text{C}$  cross-polarization magic angle spinning NMR (13C-CP/MAS-NMR).  $^{13}\text{C}$  CP/MAS NMR spectra were recorded on a Bruker AVANCE III HD-WB 400 MHz with a rotation frequency of 12 kHz.
- $\text{N}_2$  sorption isotherms.  $\text{N}_2$  (77 K) adsorption-desorption measurements were carried out on a Micromeritics Tristar 3000. Samples were previously activated for 4 h under high vacuum ( $<10^{-7}$  bar) at 120 °C.
- Thermogravimetric analysis (TGA). TGA was performed on a TGA-Q50 instrument on a platinum plate, heating the samples under nitrogen atmosphere at a heating rate of 10 °C/min.
- Dynamic light scattering (DLS). DLS studies were carried out using a Vasco 1 particle size analyser of Cordouan Technologies.
- Transmission electron microscopy (TEM). TEM micrographs and the corresponding selected area electron diffraction (SAED) patterns were recorded in a JEOL JEM 2100 TEM at 200 kV.
- Atomic force microscope (AFM). AFM was used in dynamic mode using a Nanotec Electronica system operating at room temperature under ambient air conditions. The obtained images were processed using WSxM (freely downloadable scanning probe microscopy software from [www.nanotec.es](http://www.nanotec.es)).<sup>3</sup> For AFM measurements, commercial Olympus Si/N and Ti/Pt cantilevers were used with a nominal force constant of 0.75 N/m and 2 N/m, respectively. The surfaces used for AFM experiments were  $\text{SiO}_2$  (300 nm thickness)/Si (IMS Company).
- AFM sample preparation. Freshly prepared water **NDI-COF** colloids were deposited by drop-casting on  $\text{SiO}_2$  and after 30 min dried under an Argon flow.  $\text{SiO}_2$  surfaces were

previously sonicated for 15 min in acetone, 15 min in 2-propanol and then dried under an Argon flow.

- Electrochemical measurements were carried out with a Bipotentiostat PGSTAT302N MBA (Metrohm Autolab) using the software package NOVA 1.11 (Metrohm Autolab). Static electrochemical measurements were carried out on a glass and Teflon homemade cell. Glassy Carbon (GC) electrodes ( $0.07\text{ cm}^2$  Ø with an electrochemical area of  $0.1\text{ cm}^2$ ) from CH Instruments were used as working electrodes, Pt wire as counter electrode and a homemade calomel electrode as reference electrode. Rotating disk-ring electrode (RRDE) measurements were carried out using a glassy carbon disk/platinum ring RRDE electrode from PINE and the same counter and reference electrode as in static measurements. A modulated speed rotator from PINE Instruments was used and measures were carried out in a commercial electrochemical cell adapted to rotating disc electrodes.

The GC electrodes modification was carried out by drop-casting  $80\text{ }\mu\text{L}$  of the **NDI-CON** suspension and letting it dry at room temperature.  $5\text{ }\mu\text{L}$  of  $1\text{ mg/mL}$  platinum on carbon ( $10\text{ wt\%}$ ) in  $20\%$  EtOH,  $0.02\%$  Nafion ink were drop-casted over the GC electrodes and allowed to dry at room temperature. Suspensions of  $1\text{ mg}$  of **NDI-polymer** and NDI-monomer in  $5\text{ mL}$  of Milli Q water were prepared and sonicated for 2h.  $80\text{ }\mu\text{L}$  of each suspension were then drop-casted over the disc of a GC disc/ Pt ring RRDE.

A  $15\times 15\text{ mm}$  cylindrical graphite SEM mount has been used to take the SEM images of **NDI-CON** before and after electrocatalyst. The **NDI-CON** modified graphite mount ( $80\text{ }\mu\text{L}$  of **NDI-CON** suspension in an area around  $0.1\text{ cm}^2$ ) was used as working electrode, and a potential of  $-0.5\text{ V}$  vs. calomel electrode was applied with the electrode surface immersed in a  $\text{O}_2$  saturated  $0.1\text{ M NaOH}$  solution for 3000 seconds.

HOPG plates were modified with  $80\text{ }\mu\text{L}$  of an **NDI-CON** suspension in an area of around  $0.1\text{ cm}^2$  and an AFM study of their topography before and after electrocatalyst was performed. The modified **NDI-CON** HOPG plate was used as working electrode immersed in an  $\text{O}_2$  saturated  $0.1\text{ M NaOH}$  solution, applying a potential of  $-0.5\text{ V}$  vs. calomel electrode for 3000 seconds.

## Synthesis

- **NDI-COF**: In a pyrex tube NTCDA ( $40.2\text{ mg}$ ,  $0.15\text{ mmol}$ ) and TAPB ( $35.1\text{ mg}$ ,  $0.1\text{ mmol}$ ) were suspended in a mixture of *N*-methyl-2-pyrrolidone (NMP) ( $0.75\text{ mL}$ ), mesitylene ( $0.15\text{ mL}$ ) and isoquinoline ( $0.015\text{ mL}$ ). The mixture was sonicated for 2 minutes in order to get a homogenous dispersion and the tube was degassed *via* three freeze-pump-thaw cycles, flame sealed and heated at  $120\text{ }^\circ\text{C}$  for 4 days. The precipitate was collected by filtration and washed with DMF, EtOH and THF. The resulting solid was dried at  $120\text{ }^\circ\text{C}$  under vacuum overnight to give  $64.7\text{ mg}$  ( $93\text{ }\%$ ) of **NDI-COF** as a light brown solid.

-**NDI-CONs**:  $1\text{ mg}$  of **NDI-COF** powder was sonicated in  $5\text{ mL}$  of milli-Q water for 3 h in an Elmasonic P ultrasonic bath. The resulting colloidal dispersions were centrifuged at  $500\text{ rpm}$  for 2 min to eliminate non-exfoliated **NDI-COF**.

- **NDI-polymer**: In a pyrex tube NTCDA ( $40.7\text{ mg}$ ,  $0.152\text{ mmol}$ ) and TAPB ( $35.8\text{ mg}$ ,  $0.102\text{ mmol}$ ) were suspended in a mixture of NMP ( $0.45\text{ mL}$ ), mesitylene ( $0.45\text{ mL}$ ) and isoquinoline ( $0.09\text{ mL}$ ). The mixture was sonicated for 2 minutes in order to get a homogenous dispersion and the tube was degassed *via* three freeze-pump-thaw cycles, flame sealed and heated at  $120\text{ }^\circ\text{C}$  for 4 days. The precipitate was collected by filtration and washed with DMF, EtOH and THF. The resulting solid was dried at  $120\text{ }^\circ\text{C}$  under vacuum overnight to give  $61.7\text{ mg}$  ( $86\text{ }\%$ ) of **NDI-polymer** as a dark brown solid.

## Electrochemical Methods

- Number of electrons involved in the process. For the determination of the number of electrons involved in the electrochemical process the hydrodynamic voltammograms at an **NDI-CON/GC** disc electrode were recorded at different rotation rates from 100 rpm to 1500 rpm and at the same time the Pt ring currents at 0 V vs. SCE were registered (Fig. 3b). The number of electrons involved in the ORR was calculated from equation (S1)

$$n = 4 \frac{i_D}{i_D + \frac{i_R}{N}} \quad (S1)$$

where  $n$  is the number of electrons,  $N$  is the collection efficiency of the ring (0.218 for the present geometrical arrangement) and  $i_D$  and  $i_R$  are the measured currents for the disk and ring electrodes, respectively.

- Current stability tests. A constant potential of -0.5 V vs. SCE was applied and the current was registered while keeping the rotating electrode spinning at 1500 rpm and immersed in a 0.1 M NaOH O<sub>2</sub> saturated solution.

## Theoretical Methods and Structure Modelling

We have carried out a battery of Density Functional Theory (DFT) calculations searching for the optimized ground state geometries of the 2D **NDI-COF** monolayer, as well as its associated 3D crystal structure in different stacking fashions to be directly compared with the experimental evidence.

In a first step, we have performed a preliminary DFT analysis of the two building blocks forming the **NDI-COF** in this study: 1,4,5,8-naphthalenetetracarboxylic dianhydride (NTCDA) and 1,3,5-tris(4-aminophenyl)benzene (TAPB), in order to obtain reasonable starting point geometries towards the assembling of the whole COF system. For that purpose, we have obtained optimized structures of the mentioned isolated gas-phase sub-units by the GAUSSIAN09 code<sup>4</sup> within the B3LYP/cc-pVTZ<sup>5-7</sup> level of theory.

On the basis of the preliminary optimized building blocks we have constructed the periodic model of the 2D structure to be fully optimized with the CASTEP plane-wave DFT code.<sup>8</sup> We have carried out simultaneous full lattice/cell and structure optimizations for the different 2D and 3D **NDI-COF** configurations. The calculations account for an empirical efficient vdW R<sup>-6</sup> correction (DFT+TS method).<sup>9</sup> We have used the GGA-PBE functional to account for the exchange-correlation (XC) effects<sup>10</sup> and ultra-soft pseudopotentials<sup>11</sup> to model the ion-electron interaction within the H, C, N and O atoms. The Brillouin zones have been sampled by means of optimal Monkhorst-Pack grids.<sup>12</sup> The one-electron wave-functions are expanded in a basis of plane-waves with an energy cut-off of 400 eV for the kinetic energy, which has been adjusted to achieve sufficient accuracy to guarantee a full convergence in total energy and electronic density. All the atomic relaxations were carried out within a conjugate gradient minimization scheme until the maximum force acting on any atom was below 0.02 eV Å<sup>-1</sup>. This simultaneous lattice and structural relaxation protocol provide an optimal strain minimization up to achieve a global stress < 0.01 GPa. Additionally, for the optimized 2D **NDI-COF** we have computed infinite crystal-bulk structures in both the eclipsed stacking (AA) and the staggered stacking (AB) fashions. The theoretical crystal-powder diffractograms have been simulated from the DFT-optimized structures by using the MERCURY package.<sup>13</sup>

Additionally, in order to monitor the evolution of the structure and PXRD features from the eclipsed stacking (AA) to the staggered stacking (AB), we have explored two intermediate stacking possibilities with 1/6 and 1/3 layer offsets. These two intermediate space-filling models have been DFT-computed within the same theoretical framework abovementioned. It is interesting to mention that these two intermediate interlayer



stacking models provide very similar interlayer interaction energies and yield interlayer distances of 3.57 and 3.66 Å, for the 1/6 and 1/3 layer offsets, respectively, to be compared with the values of 3.53 and 3.74 Å for the limiting AA and AB cases, respectively.

**Table S1.** Screening of conditions for the synthesis of **NDI-COF**.

<b>Solvent: NMP:Mesitylene</b>	<b>Catalyst: Isoquinoline</b>	<b>Concentration (NTCDA+TAP B)</b>	<b>Temperature (°C)</b>	<b>Activation</b>	<b>Crystallinity</b>
1/1	5 %	20 mg/mL	150	Vacuum	No
5/1	2 %	40 mg/mL	150	Vacuum	No
7/1	2 %	40 mg/mL	120	Vacuum	No
7/1	10 %	40 mg/mL	120	Vacuum	No
1/1	5 %	80 mg/mL	200	Vacuum	No
1/1	2 %	80 mg/mL	200	Vacuum	No
1/1	5 %	80 mg/mL	150	Vacuum	No
1/1	2 %	80 mg/mL	150	Vacuum	No
1/1	10 %	80 mg/mL	120	Vacuum	No
1/1	2 %	80 mg/mL	120	Vacuum	No
7/1	10 %	80 mg/mL	120	Vacuum	No
7/1	2 %	80 mg/mL	120	Vacuum	No
5/1	10 %	80 mg/mL	120	Vacuum	Low
5/1	2 %	80 mg/mL	120	Vacuum	Moderate
5/1	1 %	80 mg/mL	120	Vacuum	Moderate
5/1	2 %	80 mg/mL	120	scCO <sub>2</sub>	High

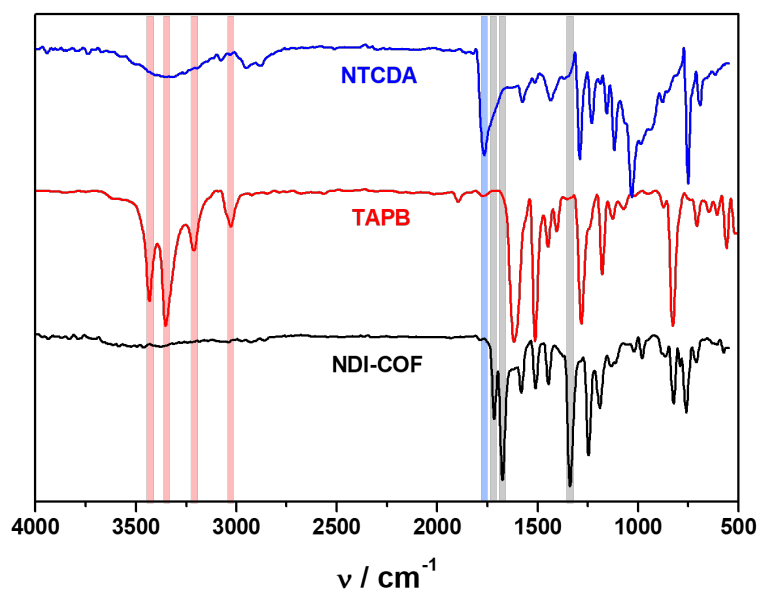


**Figure S1.** FTIR spectra of NTCDA (blue), TAPB (red) and **NDI-COF** (black) highlighting the C=O band from NTCDA (light blue), the N-H bands from TAPB (light red) and the six-membered imide ring bands from **NDI-COF** (light grey).

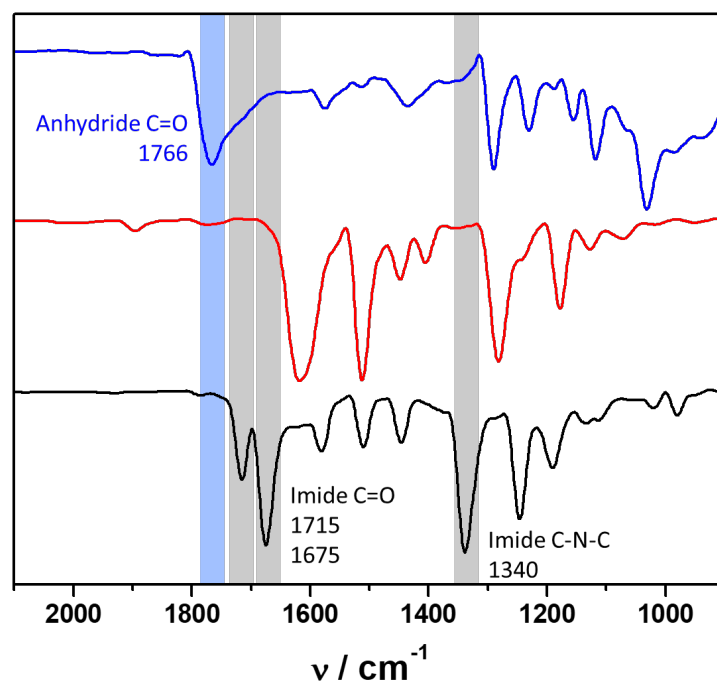


**Figure S2.** Zoomed section of the FTIR spectra of NTCDA (blue), TAPB (red) and **NDI-COF** (black) highlighting the C=O band from NTCDA (light blue) and the six-membered imide ring bands from **NDI-COF** (light grey).

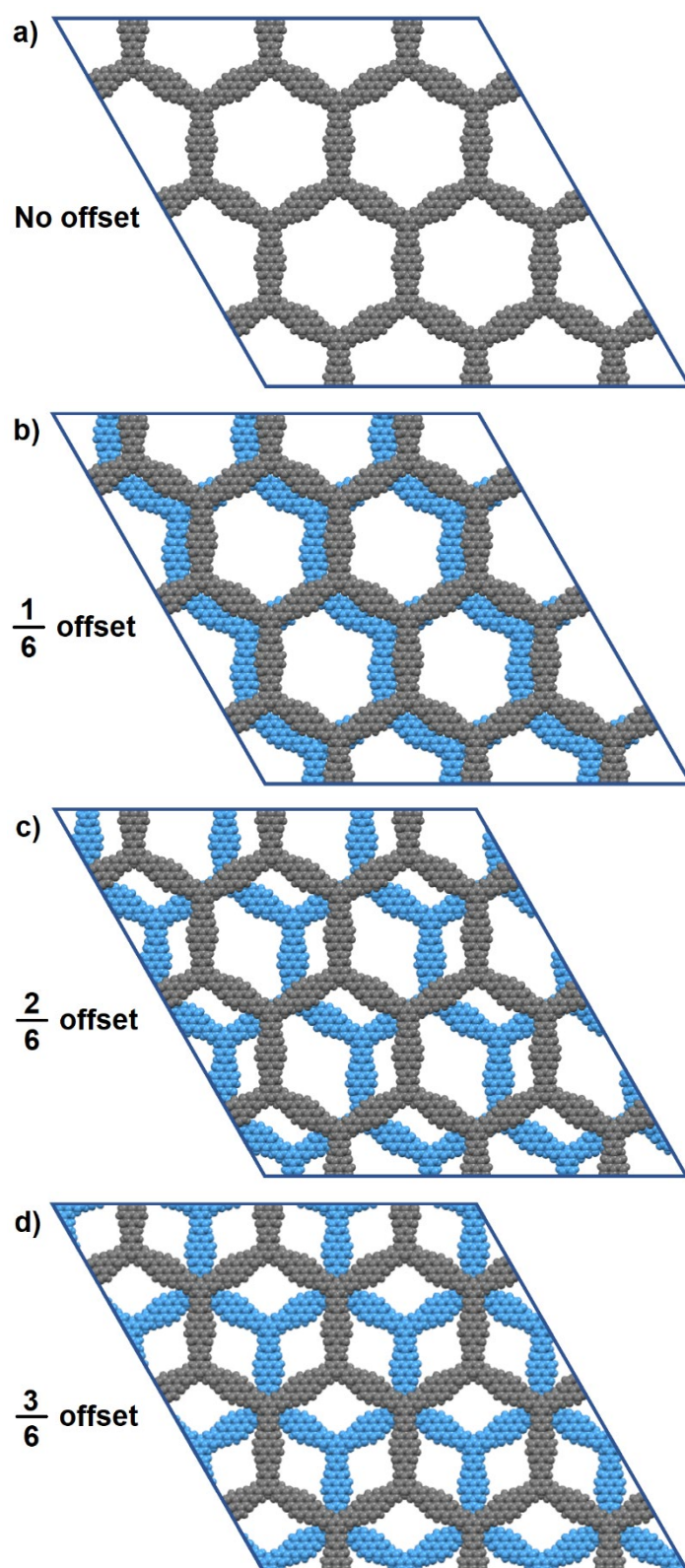


**Figure S3.** Space filling modelled structures of **NDI-COF** in the eclipsed AA stacking mode (a), with a 1/6 layer offset (b), with a 1/3 layer offset (c) and in the staggered AB stacking mode (d).

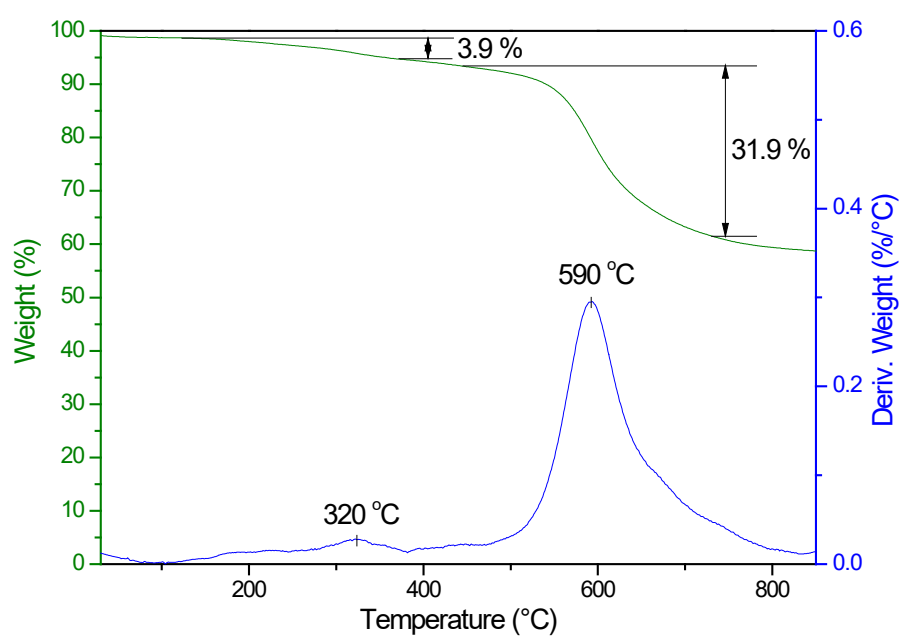


**Figure S4.** TGA curve of **NDI-COF**.

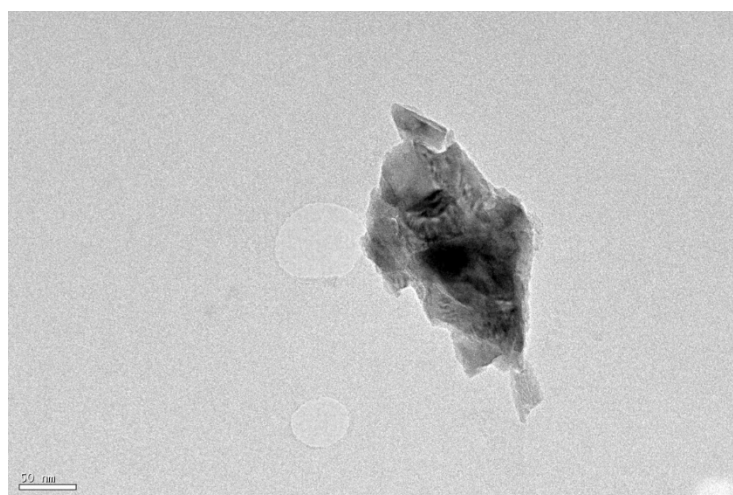
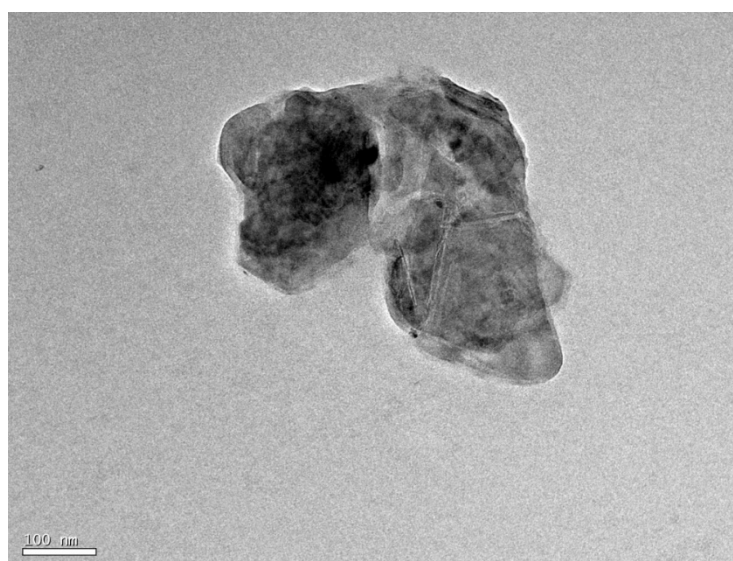


**Figure S5.** TEM images of **NDI-CONs**.

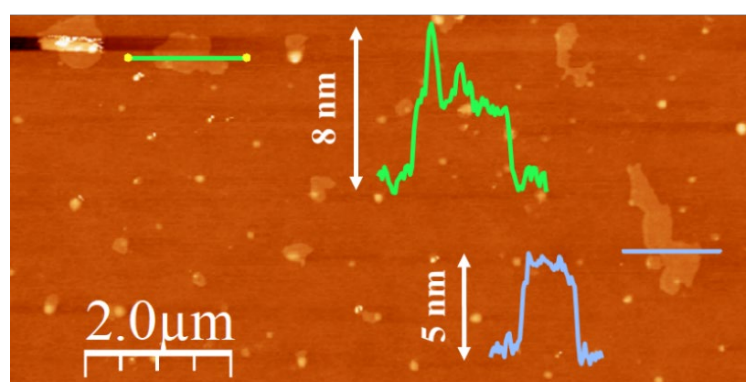
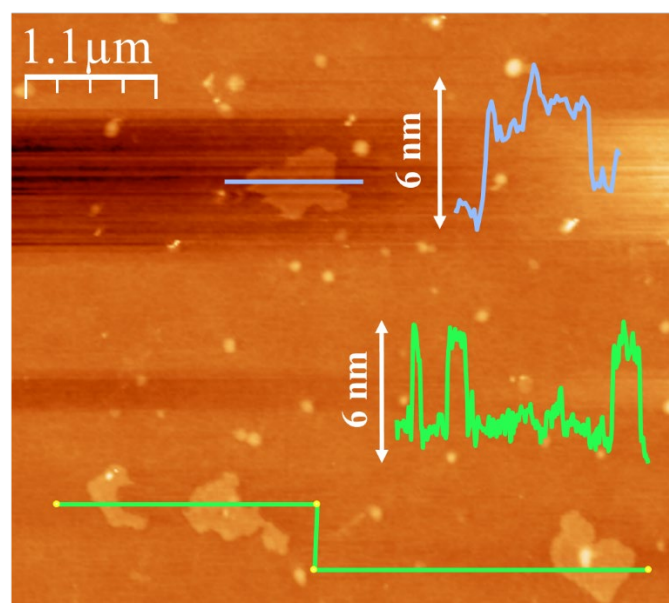


**Figure S6.** AFM topographic images and their height profiles along the corresponding lines of exfoliated **NDI-CONS**.

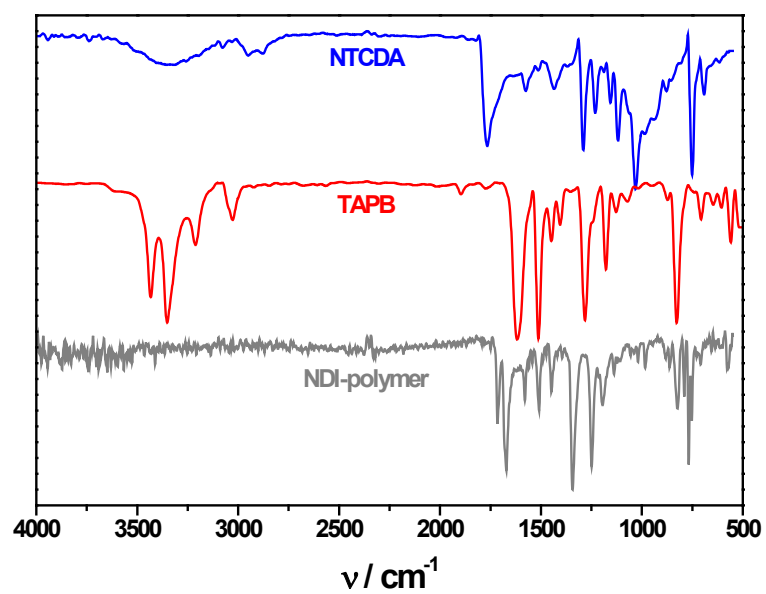


**Figure S7.** FTIR spectra of NTCDA (blue), TAPB (red) and **NDI-polymer** (black).

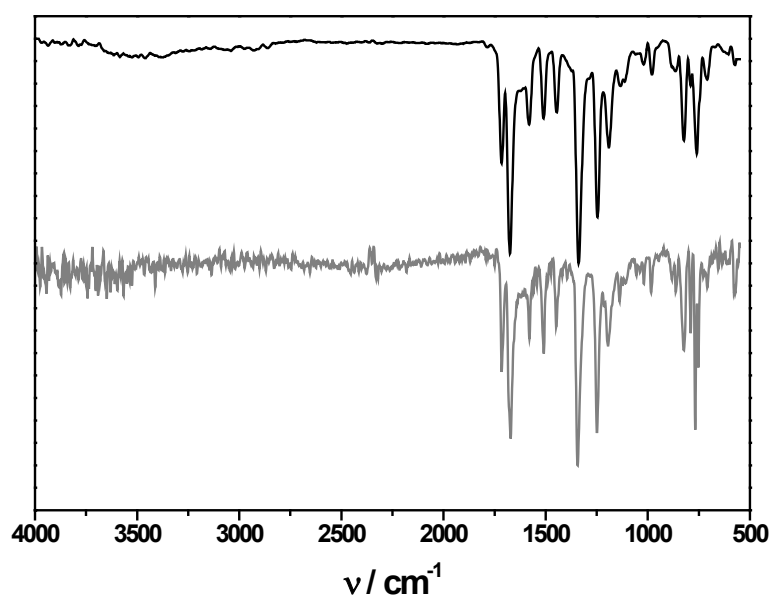


**Figure S8.** Comparative FTIR spectra of **NDI-COF** (black) and **NDI-polymer** (grey).

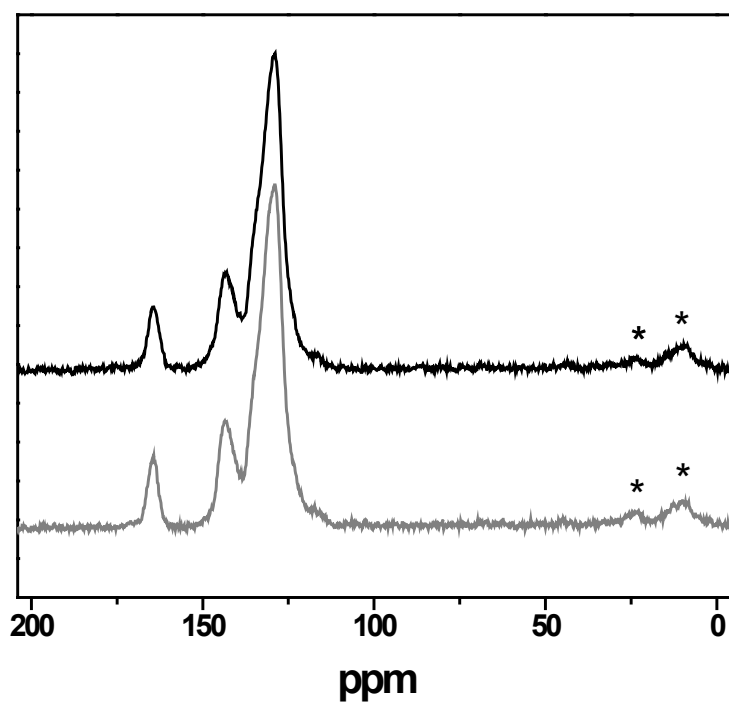


**Figure S9.** Comparative <sup>13</sup>C-CP/MAS-NMR spectra of **NDI-COF** (black) and **NDI-polymer** (grey). Asterisks indicate spinning side bands.



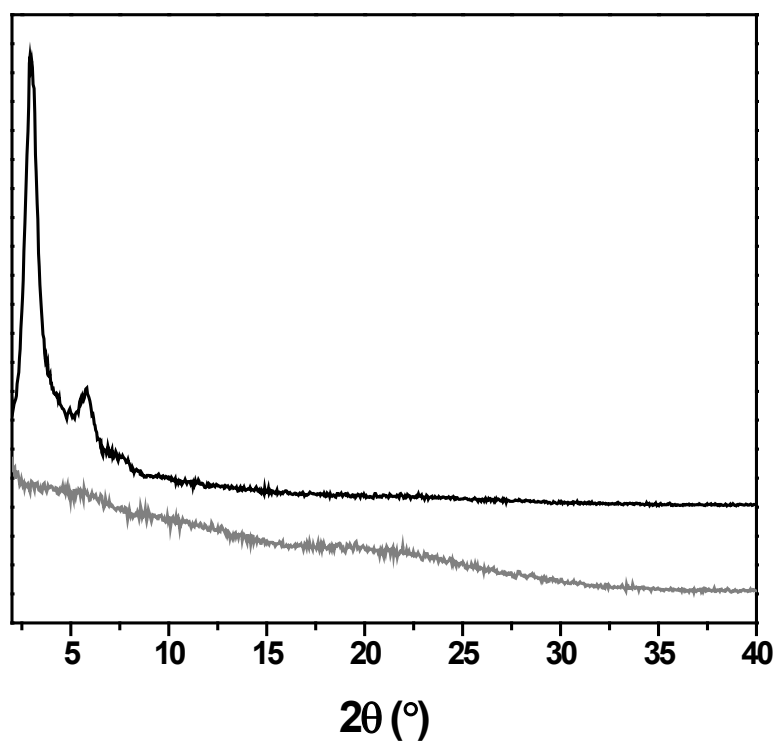


Figure S10. Comparative PXRD patterns for **NDI-COF** (black) and **NDI-polymer** (grey).

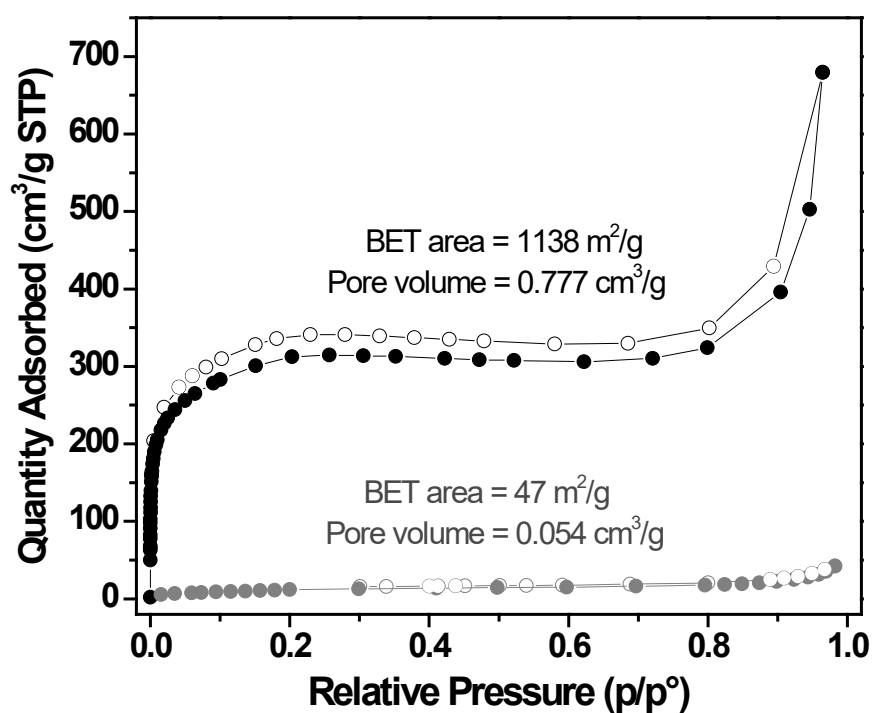
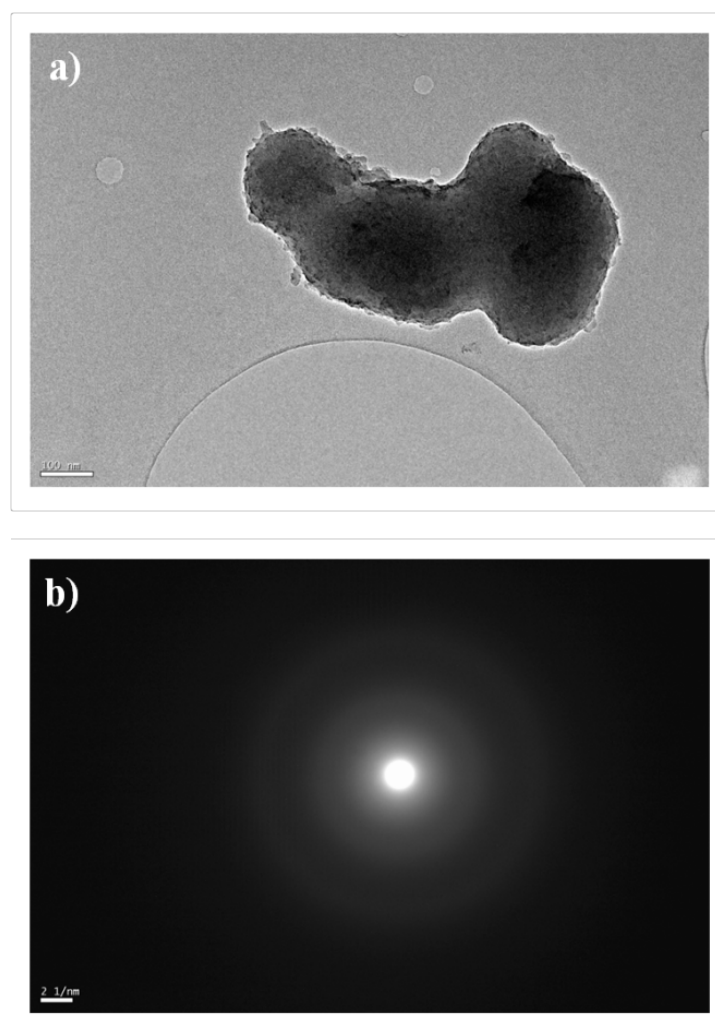
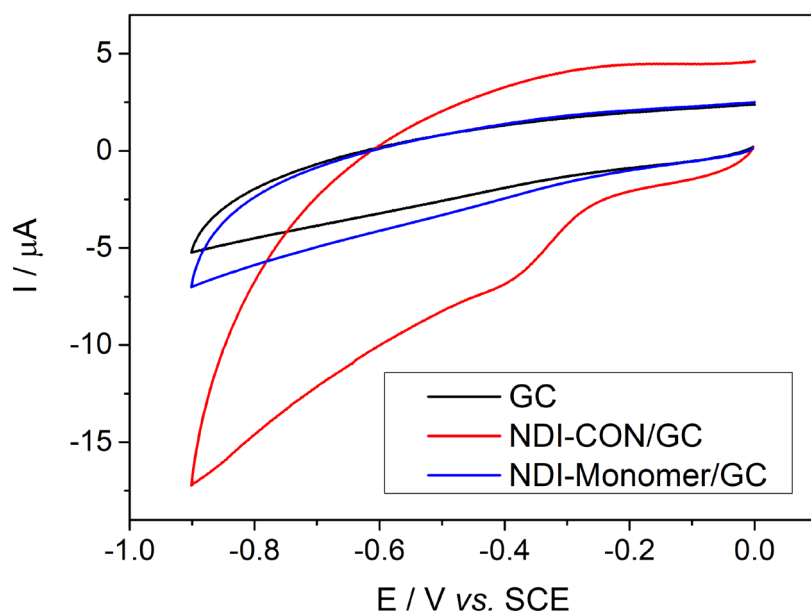


Figure S11. Comparative  $N_2$  (77 K) sorption isotherms for **NDI-COF** (black) and **NDI-polymer** (grey).



**Figure S12.** a) TEM image of **NDI-polymer** and b) its SAED analysis.



**Figure S13.** Cyclic Voltammetry of a GC electrode (black), **NDI-CON/GC** electrode (red) and a **NDI-Monomer/GC** electrode (blue) in 0.1 M NaOH N<sub>2</sub> saturated solution.

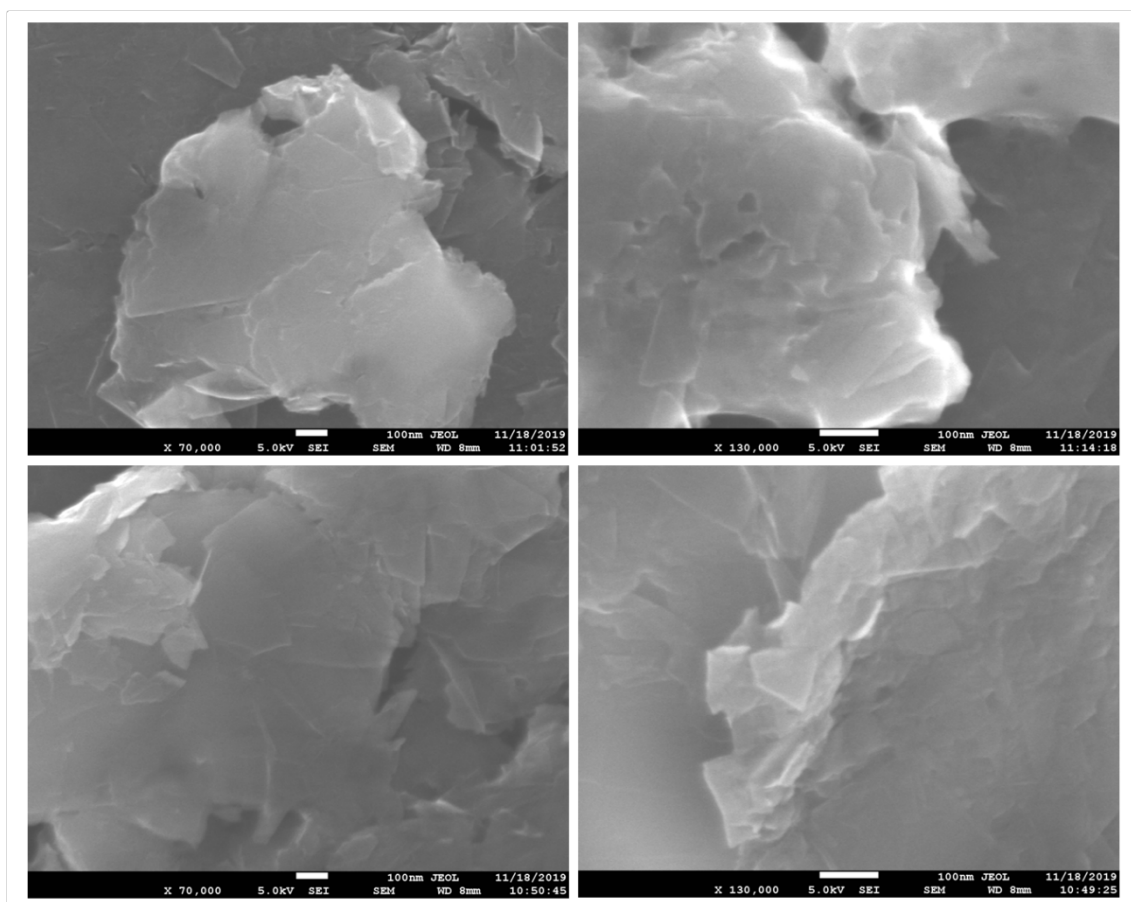


**Figure S14.** SEM images of **NDI-CONS** before (top) and after (bottom) the electrocatalytic tests.

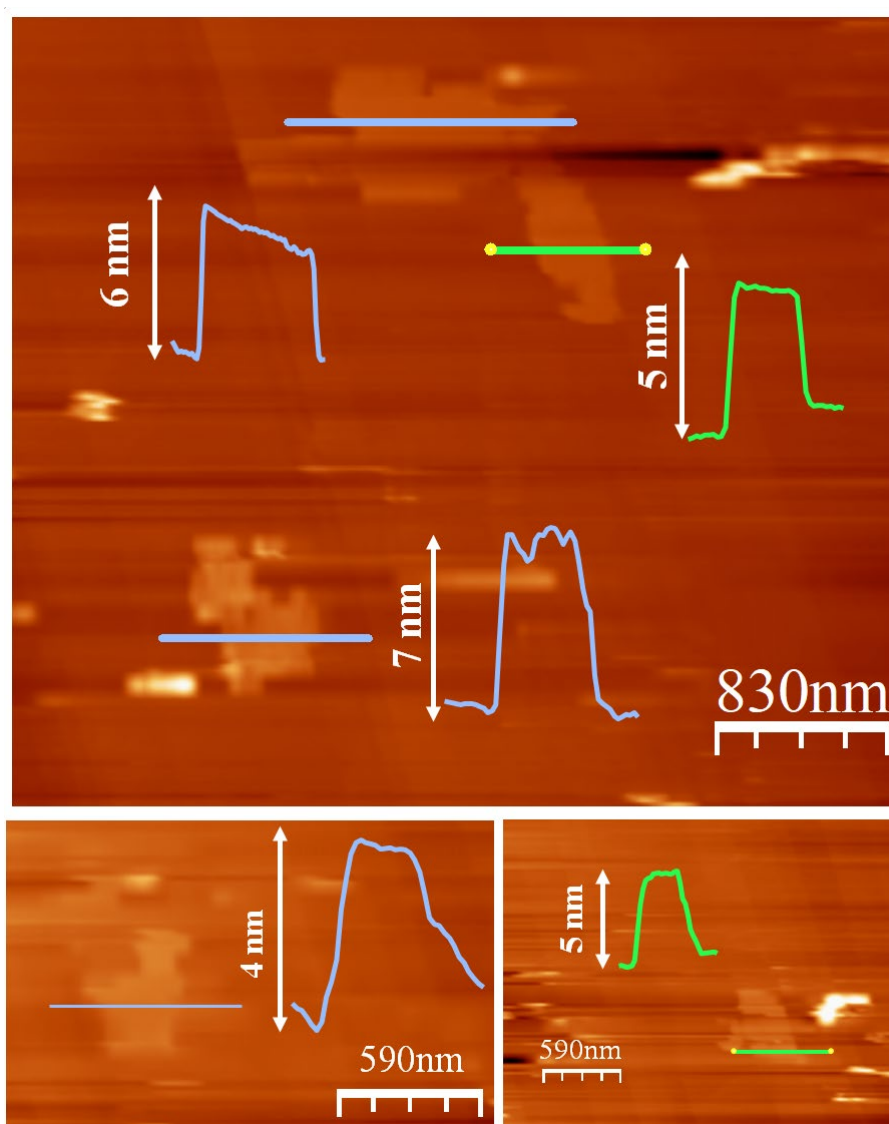


**Figure S15.** AFM images of **NDI-CONS** after electrocatalytic measurement.

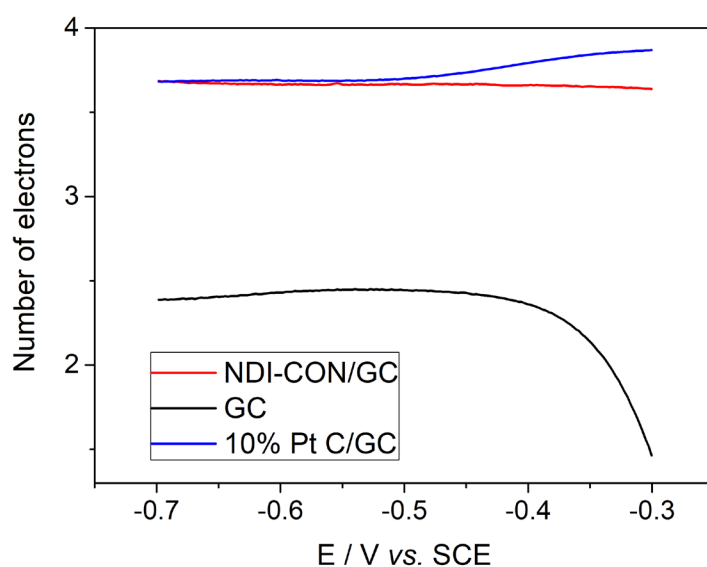


**Figure S16.** Number of electrons calculated for ORR using RRDE at different potentials at 10% Pt C/GC disc electrode (blue), GC disc electrode (red) and **NDI-CON/GC** disc electrode (black).

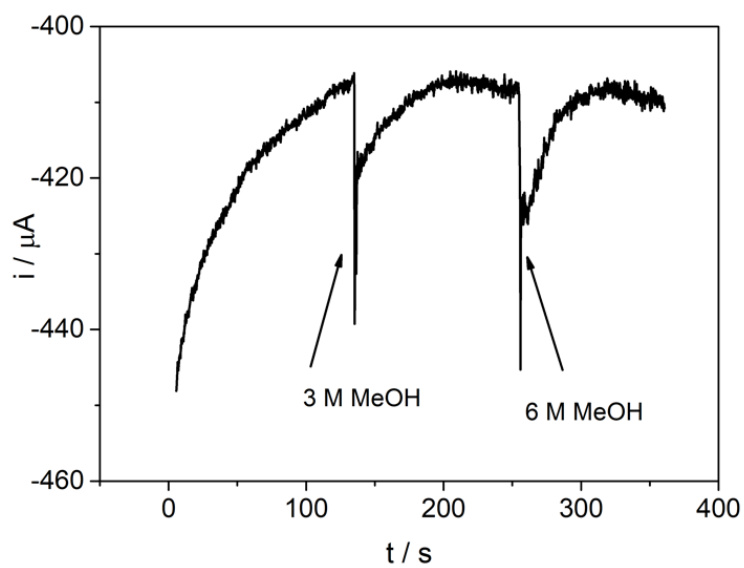


**Figure S17.** MeOH interference study of **NDI-CON/GC** electrode operating at a constant potential (- 0.5 V vs. SCE) in 0.1 M NaOH O<sub>2</sub> saturated solution.

## References

- 1 A. de la Peña Ruigómez, D. Rodríguez-San-Miguel, K. C. Stylianou, M. Cavallini, D. Gentili, F. Liscio, S. Milita, O. M. Roscioni, M. L. Ruiz-González, C. Carbonell, D. MasPOCH, R. Mas-Ballesté, J. L. Segura and F. Zamora, *Chem. Eur. J.*, 2015, **21**, 10666-10670.
- 2 S. Guo, W. Wu, H. Guo and J. Zhao, *J. Org. Chem.*, 2012, **77**, 3933-3943.
- 3 I. Horcas, R. Fernández, J. M. Gómez-Rodríguez, J. Colchero, J. Gómez-Herrero and A. M. Baro, *Rev. Sci. Instrum.*, 2007, **78**, 013705.
- 4 M. J. Frisch, G. W. Trucks, H. B. Schlegel, G. E. Scuseria, M. A. Robb, J. R. Cheeseman, G. Scalmani, V. Barone, B. Mennucci, G. A. Petersson, H. Nakatsuji, M. Caricato, X. Li, H. P. Hratchian, A. F. Izmaylov, J. Bloino, G. Zheng, J. L. Sonnenberg, M. Had and D. J. Fox, Gaussian 09, Revision A.01, 2009.
- 5 A. D. Becke, *J. Chem. Phys.*, 1993, **98**, 5648-5652.
- 6 P. J. Stephens, F. J. Devlin, C. F. Chabalowski and M. J. Frisch, *J. Phys. Chem.*, 1994, **98**, 11623-11627.
- 7 T. H. Dunning, *J. Chem. Phys.*, 1989, **90**, 1007-1023.
- 8 J. Clark Stewart, D. Segall Matthew, J. Pickard Chris, J. Hasnip Phil, I. J. Probert Matt, K. Refson and C. Payne Mike, *Z. Kristallogr. Cryst. Mater.*, 2005, **220**, 567-570.
- 9 A. Tkatchenko and M. Scheffler, *Phys. Rev. Lett.*, 2009, **102**, 073005.
- 10 J. P. Perdew, K. Burke and M. Ernzerhof, *Phys. Rev. Lett.*, 1996, **77**, 3865-3868.
- 11 D. Vanderbilt, *Phys. Rev. B*, 1990, **41**, 7892-7895.
- 12 J. D. Pack and H. J. Monkhorst, *Phys. Rev. B*, 1977, **16**, 1748-1749.
- 13 P. R. Edgington, P. McCabe, C. F. Macrae, E. Pidcock, G. P. Shields, R. Taylor, M. Towler and J. Van De Streek, *J. Appl. Cryst.*, 2006, **39**, 453-457.